High-speed x-ray reflectometry for characterization of thin film growth at high deposition rates

David Schumi-Mareček,[1] Andrew Nelson,[2] Erwin Pfeiler,[1] Maximilian Eder,[1] Florian Bertram,[3] and Stefan Kowarik[1,*]

[1]*Physikalische und Theoretische Chemie, Universität Graz, Heinrichstraße 28, Graz, 8010, Austria*
[2]*ANSTO, Locked Bag 2001, Kirrawee DC, NSW 2232, Australia*
[3]*Deutsches Elektronen-Synchrotron DESY, Notkestraße 85, 22607 Hamburg, Germany*

(Received 21 January 2025; revised 19 July 2025; accepted 4 September 2025; published 8 December 2025)

We present a high-throughput, real-time study of PTCDI-C_8 thin film growth using quick x-ray reflectivity (qXRR) with 12 ms time resolution, combined with machine learning-based analysis. *In situ* qXRR enables monitoring of vacuum deposition at growth rates from 1 to 30 Å/s, accessing a previously unexplored regime in molecular beam deposition. To efficiently analyze the resulting ∼20 000 reflectivity curves, we employ a convolutional neural network trained on a physics-informed multilayer model. This approach robustly extracts key structural parameters—including thickness, roughness, and crystalline versus amorphous content—from noisy data. We quantify interface roughness as a function of both film thickness and growth rate, identifying rapid roughening with a scaling exponent of $\beta = 0.62$ with film thickness and a secondary scaling exponent of $\gamma = 0.21$ with growth rate. Additionally, we observe a reduction in the coherently ordered film thickness and a rise in amorphous content at higher deposition rates. These results demonstrate that combining qXRR with machine learning provides quantitative access to fast kinetic growth processes, offering a powerful tool for *in situ* characterization and morphological control in organic thin film fabrication.

DOI: 10.1103/xxx9-8tk2

I. INTRODUCTION

Understanding thin film growth processes is challenging due to kinetic effects in nonequilibrium growth. While *in situ* techniques with atomic spatial and high temporal resolutions are experimentally demanding, recently developed quick x-ray reflectometry (qXRR) methods offer a promising route, enabling real-time observation of thin film growth dynamics also at high speeds [1–6]. However, despite achieving impressive time resolutions in the millisecond range and producing more than 10^4 qXRR curves for typical growth times of seconds and minutes [6], the datasets can be noisy due to the short counting times. Here machine learning (ML) [7] offers a powerful solution to deal with large datasets as well as noisy, sparsely sampled, or incomplete data [8,9]. In addition to handling noise, ML models provide near-instantaneous inference, which is critical for high-throughput and *in situ* analysis scenarios. The Neural Networks (NN) can be tailored to analyze data based on a complex model introduced through the training data [9–11]. The training of an NN is computationally expensive, so it is not particularly suited for performing a single XRR curve analysis. In contrast, for large datasets from *in situ* growth studies the initial training time is less important and the fast analysis speed makes it a compelling choice when compared to traditional curve fitting algorithms such as differential evolution [12–14].

This work deals with organic molecular layers which are used for applications in electronics [15–18] and optics [19], where well-defined film structures are key to the functionality of various devices [20,21]. Organic molecular beam deposition (OMBD) is a popular method used to fabricate ultrathin films with precise thickness control [22,23]. This technique is valuable in applications where a precise layer formation is crucial, such as in organic light-emitting diodes (OLEDs) [24,25], solar cells [26], and organic field-effect transistors (OFETs) [16,27,28]. For these devices uniform thickness, smooth surfaces, and well-ordered molecular layers, are critical for ensuring their performance [16,27,29]. However, thin film growth is a challenging process and film quality is affected by multiple parameters such as substrate structure, substrate temperature, and deposition rate [30,31].

A challenge in the formation of smooth and crystalline thin films arises from stochastic growth [32], which is governed by the random movement and adsorption of molecules on the substrate, often leading to surface roughening. Usually, a random-fractal model is used for the description of a rough surface from which follows a power law scaling relation (Family-Vicsek scaling) of $\sigma(h) \propto h^{\beta}$ where h is the average thickness or height of the film and β is the growth exponent [33]. For a statistical 'hit and stick' growth, β equals 0.5 corresponding with the highest limit for the random deposition without diffusion, while the case when $\beta > 0.5$ is denoted as a rapid roughening. Rapid roughening has been reported for systems such as the molecule diindenoperylene [34] in intermediate thickness ranges from 20 nm to 1 μm, but the scaling relation is not valid for ultrathin films of few mono-

*Contact author: stefan.kowarik@uni-graz.at

layers [35]. Rapid roughening is often observed for molecules with high aspect ratios, which tend to form rougher films with large β [36], but also inorganic materials such as the transition metal dichalcogenide MoS_2 exhibits it [37]. Rapid roughening has been investigated in a range of studies [34,37–40] and although the precise mechanism of rapid roughening remains unclear, it is believed to arise from spatial inhomogeneities caused by tilt domains of anisotropic molecular building blocks and energy barriers at monolayer step edges, which hinder adatom movement and increase surface roughness.

In addition to surface roughness, the molecular order within the layer is also important. Organic thin films can grow in a layer-by-layer fashion at least initially, but besides roughening also the growth of coherently ordered surface parallel lattice planes can break down once a critical film thickness is exceeded [41,42]. Beyond the coherent film thickness, the ordering can change to amorphous, textured polycrystalline films with high mosaicity, or a 3D powder [43]. While often crystalline layers are desirable also amorphous films can be application relevant. An amorphous layer can exhibit higher mechanical flexibility than a crystalline layer [44]. Amorphous layers are often used in OLEDs as the random orientation of molecules leads to more isotropic light emission [45–47]. The growth conditions for such tailored amorphous, polycrystalline or textured thin films are often optimized by trial and error, however, *in situ* measurement can accelerate this search. Therefore, techniques such as ellipsometry [48], x-ray reflectometry (XRR) [49], electron diffraction [50], and spectroscopy [51] are routinely employed. XRR is a nondestructive technique that provides material density, Å-level precision in measuring thin film thickness, and interface roughness [52–55]. However, its limited temporal resolution, with acquisition times in the tens of seconds [49,53,56–61] or 10 ms in highly specialized setups [4], restricts real-time monitoring of rapid film growth, leading most *in situ* OMBD studies to focus on slower evaporation rates of 0.1 to 1 Å/s [10,62].

In this work, we study roughness and crystallinity of molecular films by combining quick x-ray reflectivity (qXRR) with a machine learning-based analysis pipeline to investigate PTCDI-C_8 thin film growth at unprecedented deposition rates. Our main results are as follows: (i) We achieved real-time, *in situ* monitoring of vacuum deposition at 1–30 Å/s with 12 ms time resolution, extending XRR capabilities into a previously inaccessible kinetic regime for molecular beam deposition. (ii) We performed high-throughput structural analysis of ∼20 000 reflectivity curves using a convolutional neural network trained on a physics-informed multilayer model, enabling robust extraction of thickness, roughness, and crystalline versus amorphous content from noisy data. (iii) We quantified roughening dynamics, identifying rapid roughening with a thickness scaling growth exponent $\beta = 0.62$ and a secondary growth rate scaling exponent $\gamma = 0.21$. (iv) We observed structural transitions from crystalline to amorphous or misaligned fraction within the film at greater thicknesses and higher deposition rates. These results establish a pathway for real-time, quantitative characterization of thin film growth, with implications for process optimization and morphological control in devices.

II. EXPERIMENT

We evaporated the organic semiconductor molecule N,N'-di-n-octyl-3,4,9,10-perylenetetracarboxylic diimide (PTCDI-C_8) [63–65], which we use as a model system of organic thin film growth. The PTCDI-C_8 molecules have garnered significant attention due to their exceptional electronic properties and potential uses in organic photovoltaics, OFETs, and OLEDs. PTCDI-C_8 is an *n*-type organic semiconductor [66–69], exhibiting electron mobilities in organic thin film transistors of up to ∼1.7 cm²/Vs [66]. The molecule features a planar core flanked by two alkyl chains, contributing to its stability and functionality in ambient conditions.

To perform qXRR measurements we used the high-resolution diffraction beamline P08 at PETRA III, DESY [70], where the energy of the primary beam was set to 18 keV. We use a qXRR setup reported in Ref. [6] with a high time resolution. In short, the setup is based on the method developed by Seeck *et al.* [5], where the sample is mounted on a wedge-shaped sample holder on the top of a motor so that it wobbles. The sample holder features a wedge angle (ω_{max}) of 2°. Consequently, as the motor rotates, the sample alters its inclination with respect to the beam, ranging from 0° to 2°, depending on the specific holder used. The reflected beam is recorded on a pixel detector located behind the sample where the reflected beam makes an ellipse-like shape [Fig. S1(b) of Supplemental Material Ref. [71]]. The qXRR attains high time resolution by simultaneously collecting reflectivity data across a range of incident angles, unlike conventional XRR which scans sequentially. This parallel acquisition allows rapid measurements with temporal resolution down to the millisecond range, making it well-suited for studying dynamic processes in real time.

The experimental deposition chamber was equipped with evaporators positioned above the sample to enable *in situ* molecular beam deposition [63,72]. These evaporators were loaded with PTCDI-C_8 molecules in powder form, and the growth rate was controlled via setting a constant electric power to give the desired evaporation temperature at the crucible and monitored through Quartz Crystal Microbalance (QCM) readings. For this experiment, we modified a hard drive motor to operate under high vacuum conditions (2.5×10^{-6} mbar) and we mounted it into a portable vacuum chamber for OMBD [29,72,73]. This chamber was extensively modified to accommodate the motor, including a light barrier to read the rotation speed which is necessary to trigger the detector read-out and measure the rotation frequency.

We maintained a constant rotation speed of 40 Hz on the motor for all experiments. We recorded two qXRR curves per 25 milliseconds, with each single qXRR curve obtained within 12.5 milliseconds. Given that the reflectivity spans a very large intensity range across several orders of magnitude, we placed a fixed set of absorbers in front of the detector to capture the full reflectivity curve accurately within the available dynamic range of the detector. Due to the absence of slits between the sample and the detector, air scattering significantly contributed to background noise despite a beam-stop shortly after the sample. To mitigate this, we read out the detector every millisecond, which reduced the acquisition of background noise as compared to 12.5 ms integration times

for a full qXRR curve. Consequently, the final qXRR curves were reconstructed from multiple 1 ms detector images in which short 'signal stripes' were visible corresponding to small q-range sections of the complete XRR curve [Fig. S1(a) [71]].

All experiments were conducted on silicon wafers which had a silica layer of 45 Å thickness. Samples were cut from the wafer using a laser cutting machine and cleaned in an ultrasonic bath with acetone and isopropanol. The dried silicon wafer was mounted onto the sample holder using double-sided carbon tape suitable for vacuum environments (Labtech). The sample holder with the silicon substrate was then mounted onto the motor. During setup, the sample was covered with a light aluminum shutter that flew off once rotation started, allowing us to establish the desired molecular deposition rate before starting measurements. We investigated molecular deposition rates ranging from 1 to 30 Å/s, conducting seven experiments.

The detector data extraction pipeline was similar to the pipeline described already in our previous work [6]. In short, the data were analyzed using a Python script (see data availability statement) where the ellipse-like shape of the specular beam on the detector was analyzed and fitted according to its shape, where the shape is given by $\omega_{\max}$ (steepness of the sample holder). Although $\omega_{\max}$ is constant, the mounting of the sample can introduce a slight offset as the sample may not be perfectly parallel to the holder. Once the elliptical shape was fitted, the XRR curve was extracted and normalized. This included corrections for angular speed variations and therefore different exposure times at different angles, absorber correction, and footprint correction. In this publication, we made several modifications with respect to the processes in Ref. [6] due to the reconstruction of qXRR curves from multiple 'signal stripes.' The 'signal stripes' where created by 1 ms integration time and consequently one XRR curve was made as a stack of 12 'signal stripes' (Fig. S1 [71]). First, we developed a script to detect when a reflectivity edge appeared on the detector. Subsequently, we extracted nine subsequent and two previous 'stripes' since a single XRR measurement took 12.5 ms. We mapped pixels to corresponding q values and extracted the highest measured value for each q value. Due to two–three pixel gaps between 'stripes,' our algorithm identified and removed these gaps, then extrapolated data from neighboring q values (Fig. S1 [71]). One limitation of this method was that the read-out capacity of the setup was limited to 2000 images, covering only 2 seconds of thin film growth. Additionally, communication between the data storage and the detector required 10.5 seconds, resulting in noncontinuous data collection from the formation of the PTCDI-C_8 thin layer (as shown in Fig. 2 and Figs. S4–S10 [71]).

III. PHYSICS-INFORMED STRUCTURAL MODEL

We utilize a physical parametrization for a complex multilayer structure to represent the growth dynamics of thin films with a limited number of parameters [10]. The sample consists of a silicon/silicon oxide substrate topped with a thin film composed of repeating identical PTCDI-C_8 monolayers, each consisting of regions with higher scattering length densities (SLDs) at the molecular core and lower SLD for the side chains. The structure of the thin film is further modeled using two sigmoid/error function [74]) envelopes. A total sigmoid envelope cuts the SLD profile of the monolayers, defining the total film thickness and the roughness at the top interface. It helps in modeling the gradual transition in SLD from the bulk of the film to the vacuum SLD, accounting for surface roughness. A second sigmoidal envelope modulates the SLD contrast for describing a coherently ordered, crystalline part of the multilayer. It enables the representation of a film that is coherently ordered up to a certain thickness, beyond which it becomes incoherently ordered or amorphous (Fig. S2 [71]) (see also Refs. [12,75,76] therein). This scenario is often observed when Kiessig's and Laue's fringes display different periodicities.

Additionally, a 'phase layer' is introduced between the substrate and the multilayer. This layer accounts for the PTCDI-C_8 side chains in contact with the substrate and the interface structure, which might differ from the multilayer period. The phase layer is crucial as it significantly influences the scattering phase relationship between the substrate reflection and the Bragg reflection, affecting the shape of the curve around the Bragg reflection due to constructive or destructive interference [11].

The model has 17 parameters: 3 describing the substrate, 3 describing the phase layer, and 11 describing the multilayer [10]. However, due to the high-dimensional parameter space, predicting these parameters from noisy experimental data is challenging [9]. To achieve better model performance, we restricted the parameter space and implemented the complex multilayer structure model into the refnx [12] fitting algorithm, enabling the extraction of all parameters from a refnx fit. This approach allows us to extract substrate and phase layer parameters from a standard XRR measurement with a low-noise background. With determined parameters for the phase layer and substrate, we trained the neural network with only seven parameters, significantly improving the efficiency and performance of our neural network model. The parameter ranges are shown in Table I.

The rest of the parameters were set as constants. Namely, parameters for silicon, silicon oxide, and the phase layer. The silicon parameters were SLD = 21.861 10^{-6} Å^{-2} and roughness = 1 Å. The silicon dioxide parameters were used as SLD = 21.2632 10^{-6} Å^{-2}, roughness = 1.2 Å, and thickness = 47 Å. Finally, the phase layer parameters employed were SLD = 16.7 10^{-6} Å^{-2}, roughness = 7.8 Å, and thickness = 5.3 Å. These constant parameters were determined from the refnx fit to constrain the training parameter space for the NN.

IV. NEURAL NETWORK

In our study, we evaluated several established neural network architectures, including the standard Dense Neural Network [7], 1D Convolutional Neural Network [77], ResNet [78], DenseNet [79], and EfficientNet [80]. Among these, the DenseNet-BC architecture provided the best and most consistent performance with our experimental data. We used a normalized XRR curve as input for the neural network and opted for 1D convolutional layers. The optimal architecture was identified by the validation performance and stability on

TABLE I. Parameter ranges for the neural network training and refnx prediction. Values fitted with refnx and predicted with NN for a thin film after the growth at a deposition rate of 1 Å/s (Fig. 1).

Variable	Fit range	Refnx fit	NN prediction
Monolayer thickness [Å]	[18,27]	20.84 ± 0.01	20.76
SLD low [10^{-6} Å^{-2}]	[2,9]	8.2 ± 0.3	6.95
Difference between SLD high and SLD low [10^{-6} Å^{-2}]	[4,14]	7.7 ± 0.2	11.72
Total film thickness [monolayers]	[−0.5, 30]	23.9 ± 0.1	23.32
Roughness [monolayers]	[0.1, 5]	0.62 ± 0.02	0.77
Coherent film thickness [monolayers]	[−3, 31]	23.3 ± 0.8	23.3
Coherent layer roughness [monolayers]	[0.1, 4]	2.6. ± 0.3	0.15

the experimental data set. The architecture consisted of five dense blocks with depths of [4,4,6,6,10] 1D convolutional layers interconnected by transition layers, a growth rate $k = 12$ and a compression factor $\theta = 0.7$. Additionally, it featured a flatten layer followed by a multilayer perceptron (MLP) [81]. To enhance performance, each dense block's output was flattened and then fed into a separate MLP. The MLPs outputs were concatenated to create a tensor that was channeled to our seven outputs (Fig. S14 [71]). We used the GELU [82] activation function for hidden layers, the sigmoid activation function for the output layer and the Adam [83] optimizer.

We trained the neural network using data generated with refnx. Initially, we set the boundaries for the open parameters as specified in Table I. The generated data were then augmented to reflect the same noise distribution observed in the experimental data. We added Poisson noise, using the maximum counting statistics derived from the measurement, and introduced background noise to the simulated data. This data augmentation process significantly improved the model's performance on the experimental data. We generated a dataset of $\approx 10^7$ XRR curves that fit on our GPU VRAM (Nvidia GeForce RTX 2080 Ti) and trained the neural network for 10 epochs. The size of the validation data set was 10^6 XRR curves. We used Python programming language and the GPU-integrated TensorFlow [84] library for our NN architecture.

We used the prediction made by the trained neural network as starting parameters for the multilayer structure model in refnx. The Neural Network provides an immediate guess for the thin film parameters that are close to the ground truth [85–91]. Ground truth refers to the known parameter values used to assess prediction accuracy. These values are exact for synthetic data and approximated using growth rate–thickness trends in experimental data.

This resulted in improved fitting quality and faster fitting times. However, the accuracy of predictions for thin films with just one to three monolayers was limited due to the complexity of the multilayer structure model. The neural network had difficulty predicting accurate parameters when the Bragg peak was missing or when the sigmoid representing coherent layer growth was defined by only one or two monolayers. Conversely, the neural network performed better than refnx for very thick layers, where oscillations become narrower and harder to distinguish from noise (Fig. S3 [71]). Additionally, the neural network's prediction speed was significantly faster (a few milliseconds per curve) compared to traditional fitting methods (which usually takes more than ten seconds). However, conventional fitting methods have the advantage of not requiring training or data generation. Given the size of our datasets, which include thousands of XRR curves, we chose to use the NN prediction as our primary method due to its significant speed advantage of 5 ms per prediction compared to ∼10–100 seconds from refnx fits and we used refnx fits only with NN starting values for exemplary fits shown in the manuscript.

In our data analysis, we utilized NN prediction as the primary tool, specifically employing a DenseNet architecture. This choice was driven by the speed of the NN predictions and their superior performance on noisy data. Traditional methods like refnx with a multilayer model often encounter challenges when analyzing thicker films deposited at higher growth rates. In such cases, it becomes difficult to distinguish actual oscillations from noise introduced by factors such as absorber edges, gaps between stripes, and interpolation errors. As a result, refnx may tend to fit higher values for total and coherent roughness, which can suppress the oscillations. This issue is not inherently due to the fitting algorithm itself but rather stems from the limitations of the model, where certain parameters can correlate, leading to incorrect fits [as demonstrated in Supplemental Material Fig. S3(a) [71]]. Such fitting issues can be mitigated by either constraining the parameter space or setting the initial values of the fit closer to the expected results [Fig. S3(a) [71]] (see also Refs. [34,36,38,92] therein).

V. RESULTS

A. Standard postgrowth XRR

Figure 1(a) shows postgrowth XRR measurements using standard diffractometer scans on a 500 Å PTCDI-C_8 thin film grown at a slow growth rate of 1 Å/s. We fit the standard, low-background XRR data with refnx where the initial values were defined by the NN prediction [Fig. 1(a) (red)]. We also show the NN prediction on the same XRR curve [Fig. 1(a) (orange)]. In Fig. 1(b) we compare the corresponding SLD profiles for the refnx fit (red) and the NN prediction (orange).

Overall, the NN fit and refnx fit yield similar structures, with the SLD profiles showing PTCDI-C_8 layering, similar film thickness and roughness. However, refnx finds a better fit using a layer that is one monolayer thicker. As the NN is trained on noisy data of qXRR, the performance on this low-noise postgrowth XRR is not as good as the refnx fit

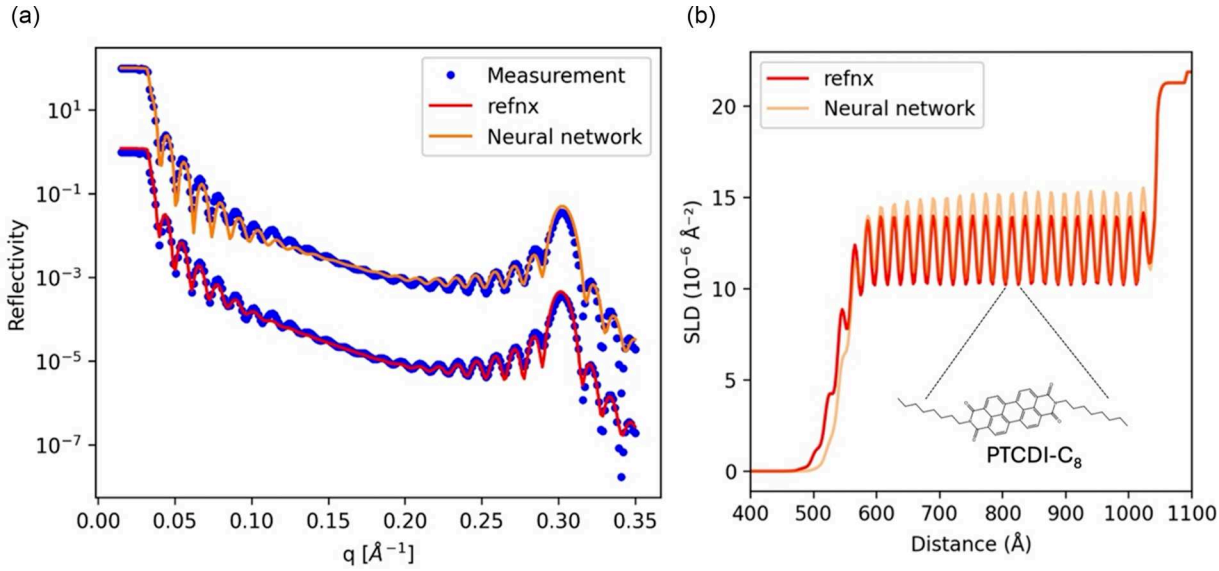

FIG. 1. A comparison of the refnx fit and NN prediction on the standard 400-second long XRR measurement of a thin PTCDI-C_8 film using the same multilayer structure model. (a) refnx fit of the measurement (red) and the NN prediction (orange). (b) Corresponding SLD profiles of the sample for the refnx fit (red) and the NN prediction (orange). The inset shows the chemical structure of PTCDI-C_8 with dashed lines indicating the size of the molecular core and the interdigitating side chains in the SLD profile.

with the NN results as starting values. This in part explains the lower prediction quality of the NN for the oscillations beyond the Bragg peak [Fig. 1(a)]. The fitted and predicted parameters of the thin film layer are shown in Table I. The parameters are mostly comparable apart from a difference in SLD contrast where the NN predicts higher SLD. In the Supplemental Material (Fig. S3 [71]), we provide a comprehensive comparison of the refnx fit without NN initial values, the NN prediction, and the refnx fit with NN starting values on the qXRR curve measured during thin film deposition at 2 Å/s. This comparison demonstrates that the NN prediction is close to the true solution and can generate predictions for a single XRR curve within a few milliseconds. The refnx fit with NN starting values achieves closer alignment between fit curve and experimental data but requires several minutes to process a single XRR curve. In addition to the speed advantage of NN over refnx, the NN approach performs better when analyzing thicker films with multiple narrow oscillations. This may be due to several factors. The NN was trained using noisy data, where the noise and missing data profile was designed to mimic experimental conditions, including absorber edges, stripe gaps, background noise, and interpolation artefacts. Therefore, the training allowed the NN to more accurately handle the complexities of the data, providing a robust alternative for analyzing thicker films where traditional methods may struggle.

B. *In situ* measurements

We performed experiments where we grew PTCDI-C_8 thin layers with seven different growth rates to give insight into the growth dynamics, beyond the available studies that have so far only worked at slow deposition rates due to limited XRR acquisition times. We varied the growth rate from 1 to 30 Å/second throughout the experiments while the XRR time resolution was fixed with one qXRR curve measured in 12.5 milliseconds. Here we exemplarily show the data predicted by the NN from the experiment with the slowest growth rate of 1 Å/second as the data set has the largest number of curves (Fig. 2). The experiments at all other rates are shown in the Supplemental Material (Figs. S3–S9 [71]). A single neural network was used across all experiments, with substrates sourced from the same wafer to maintain consistency. Note, that even for the slow growth rate, the fast acquisition speed is beneficial as the film thickness is not changing during a single measurement. This compares favorably to standard XRR measurement where the measurement time is significantly longer and the change of the thickness during a single XRR scan must be considered [10].

The data consists of multiple data clusters, each cluster consisting of 37 qXRR curves with a 10.2 second delay between clusters due to the internal detector memory and detector readout speed at the beamline at the time of the experiment. Figure 2 shows the most important parameters of the model as a function of molecular exposure which corresponds to growth rate times deposition time. It is equivalent to the deposited film thickness in the case of a 100% sticking coefficient. The total and coherent thickness [Fig. 2(c)] are calculated from the relative position of the total and coherent sigmoid, respectively. Similarly, the total roughness [Fig. 2(d)] is derived from the relative widths of the total sigmoid.

The total as well as the coherent thickness [Fig. 2(c)] agree at the beginning of the growth, while for a thicker film the coherent thickness trails the absolute thickness with a small gap, which indicates a thin amorphous or untextured layer forming so that the film is no longer fully coherently ordered.

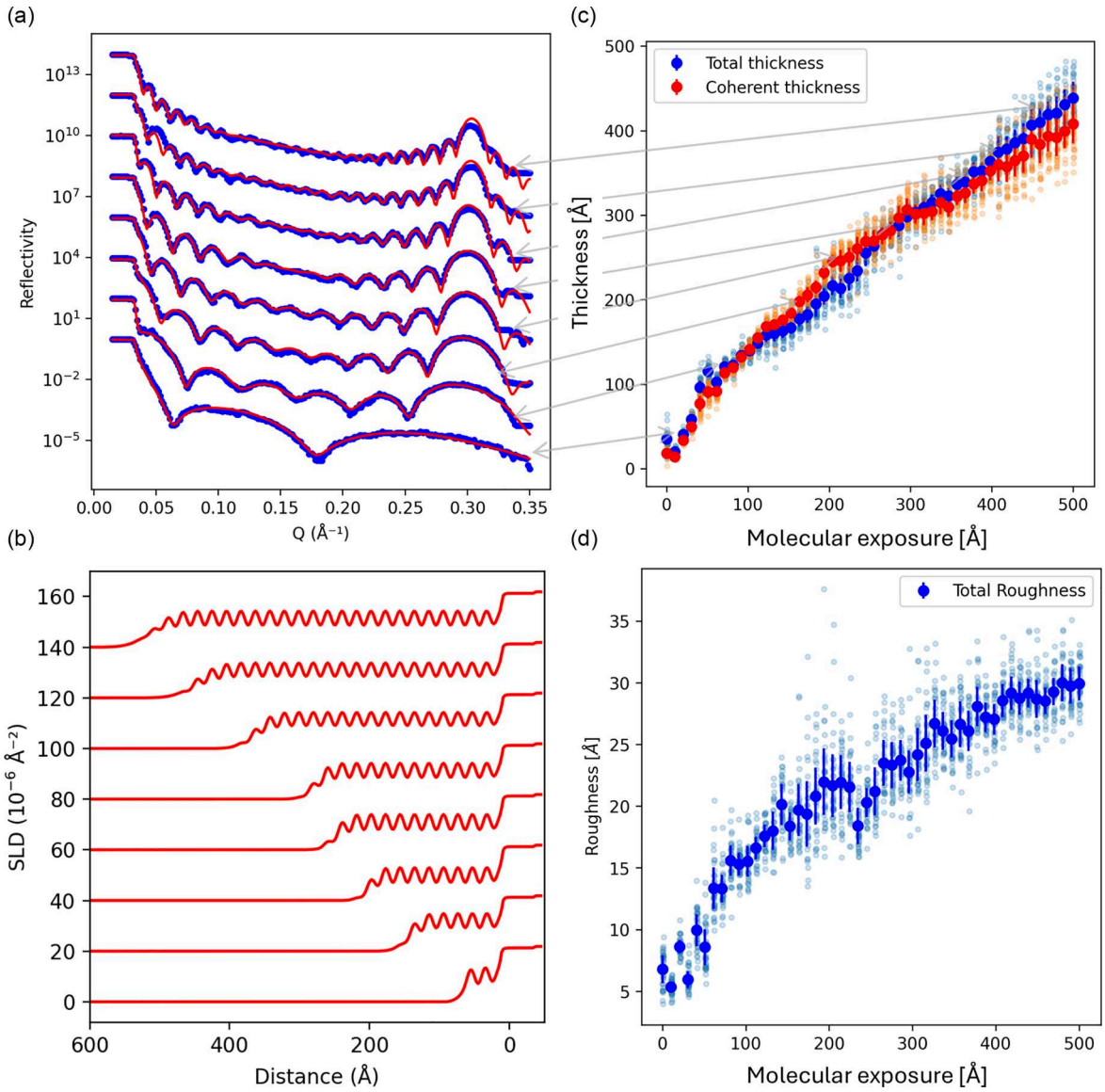

FIG. 2. Growth of the thin PTCDI-C_8 layer under the growth rate of 1 Å/second. (a) Neural network prediction polished with refnx fit of sample curves recorded within 12 ms each during the growth. (b) Corresponding SLD profile of the sample curves indicating the formation of the layers. (c) The evolution of the absolute (blue) and coherent (orange) thickness, mean value, and MAE variation is shown in the plot. (d) Absolute roughness as a function of the molecular exposure where mean value and MAE variation are shown.

The total roughness as shown in Fig. 2(d), increases with a thicker layer, which can be described by a scaling law

$$\sigma \sim t^{\beta}, \tag{1}$$

where σ is roughness, t is thickness and β is a growth exponent [34,93–95].

Since the growth contains ∼2200 qXRR curves, we present a small selection of measured and fitted qXRR curves in Fig. 2(a). The fitting process uses the trained neural network, with its predicted parameters serving as the initial guess for refinement using the refnx fit. This approach greatly enhanced the performance of the refnx fit, especially on quickly measured noisy data where fitting with a complicated model function might otherwise fail. Alongside the fitted qXRR curves, Fig. 2(b) displays the corresponding SLD profile of the sample where we see the formation of individual molecular monolayers as described by the structural model.

We analyzed all the experiments in a similar manner, extracting the seven predicted parameters and plotting them as a function of the molecular rate (see Figs. S4–S10 [71]). Additionally, we extracted the total roughness as a function of the total thickness, which can be fitted with the above scaling law. However, as shown in Fig. 4, roughness increases not only with the layer thickness but also as a function of the growth rate. This behavior cannot be described in the Family-Viscek scaling theory framework, so we extend it using a second, phenomenological scaling relation as a function of growth rate Gr with an exponent γ. The data can be fitted with a double exponential function [93,96–98]

$$\sigma(t, Gr) \sim t^{\beta} \cdot Gr^{\gamma}. \tag{2}$$

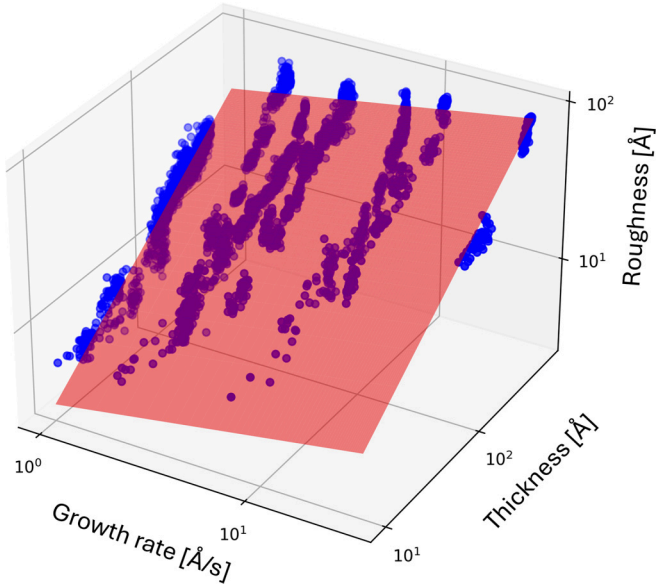

FIG. 3. Roughening of a thin layer as a function of the thickness and growth rate. The red plane is a fit using the scaling relation of Eq. (2). The fit uses NN roughness predictions of all XRR curves within our study.

Using this function and data from experiments conducted at different growth rates, we can model roughness as a function of both thickness and growth rate (Fig. 3). The red plane in the log-plot shows the functional fit with Eq. (2), and the fitted parameters are $\beta = 0.62$ and $\gamma = 0.21$. Our measurement finds a value $\beta = 0.62$, indicating so-called rapid roughening, that is faster roughening than the random deposition limit, with $\beta = \frac{1}{2}$ [99]. The exact fit value for γ depends slightly on the used data. When we used averaged roughness instead of all predicted values, parameters were determined as $\beta = 0.61$ and $\gamma = 0.24$. While Fig. 3 shows an overall fit of all growth rates with the scaling description of Eq. (2), we also fitted the roughness as a function of thickness for each experiment independently (Fig. S11 [71]). Assuming a constant proportionality constant of 0.77 and $\gamma = 0.21$, we extracted the growth exponent β for each experiment, yielding $\beta = 0.62 \pm 0.03$.

C. Coherent thickness and amorphous content

We consistently observed from the experimental data that the ordered fraction of the film diminishes with higher growth rates (see Fig. S13 [71]). In Fig. 4(a), the coherent thickness is plotted as a function of molecular exposure for all experimental growth rates. As growth rates increase, the growth speed of the coherent part diminishes, and the final coherently ordered film thickness decreases. Figure 4(b) presents the SLD profiles corresponding to qXRR curves obtained during slow growth, where the layer is nearly entirely crystalline (see Fig. 2). Conversely, Fig. 4(c) illustrates the SLD profiles of films formed at higher growth rate of 12 Å/s, showing the development of a noncoherently ordered film on top of the coherently ordered thin film. This lack of coherently ordered lattice planes as visible in the SLD modulation can have its origin either in an amorphous film on top of the crystalline bottom layer, or a high mosaicity. A high mosaicity or a loss of preferential orientation (texture) leads to an averaged, smooth SLD profile so that we do not observe substrate parallel layering in PTCDI-C_8 films. The colored areas in Figs. 4(b) and 4(c) serve as a visualization of the coherently ordered regions of the thin film. Interestingly, for all films, we find a tendency of the ordered film thickness to saturate beyond a certain thickness. This indicates that all films grow in an amorphous or high mosaicity fashion after a certain thickness. However, this critical thickness beyond which the coherent film thickness does not grow depends strongly on the deposition rate, with 30 Å/s having only about 50% the coherently ordered film thickness as compared to a rate of 1 Å/s.

VI. DISCUSSION

To unravel the interplay between deposition conditions and the structural and morphological evolution in organic semiconductors, we investigated the growth dynamics of PTCDI-C_8 thin films using *in situ* qXRR combined with machine learning. We find that the surface roughness scales with both film thickness and growth rate as $\sigma(t, Gr) \sim t^{0.62} \cdot Gr^{0.21}$, and observe a transition from highly ordered crystalline layers to films with high mosaicity or amorphous character between 250 and 400 Å as the growth rate increases from 1 to 30 Å/s. These insights have direct implications for the design of optoelectronic devices, where surface roughness and crystallinity critically influence charge transport, exciton diffusion, and light emission. Precise control over deposition parameters – particularly growth rate and film thickness – enables the targeted engineering of film morphology to optimize device performance. Importantly, the extracted growth exponents provide predictive power for tuning morphological features across different processing regimes. While organic semiconductor layers are essential in devices such as OLEDs and OFETs, they also function as transport or blocking layers in hybrid systems with materials like perovskites. Understanding and controlling their growth behavior is therefore crucial for optimizing both fully organic and hybrid optoelectronic devices.

Beyond specific material or device implications, this study enriches the fundamental understanding of scaling approaches in molecular film growth. By systematically exploring a wide range of deposition rates enabled through our *in situ* qXRR, we introduce a phenomenological scaling law explicitly connecting roughness and growth rate: as $\sigma(Gr) \sim Gr^{0.21}$. While purely phenomenological, this scaling law extends the original Family–Vicsek theory, itself reliant on *ad-hoc* assumptions of self-affine random fractal surface geometries. The random fractal approach only holds at intermediate length scales, but clearly self-affine shapes stop at atomic length scales and the fractal description is also not accurate on macroscopic scales. Despite these inherent limitations and their phenomenological nature, scaling laws remain instrumental tools for characterizing kinetic roughening phenomena and our extension of Family–Vicsek scaling recognizes that real systems may have rate-dependent effects.

Rapid roughening is found independent of growth rate, in line with previous studies of other organic thin films. Following the discussion of rapid roughening in Refs.

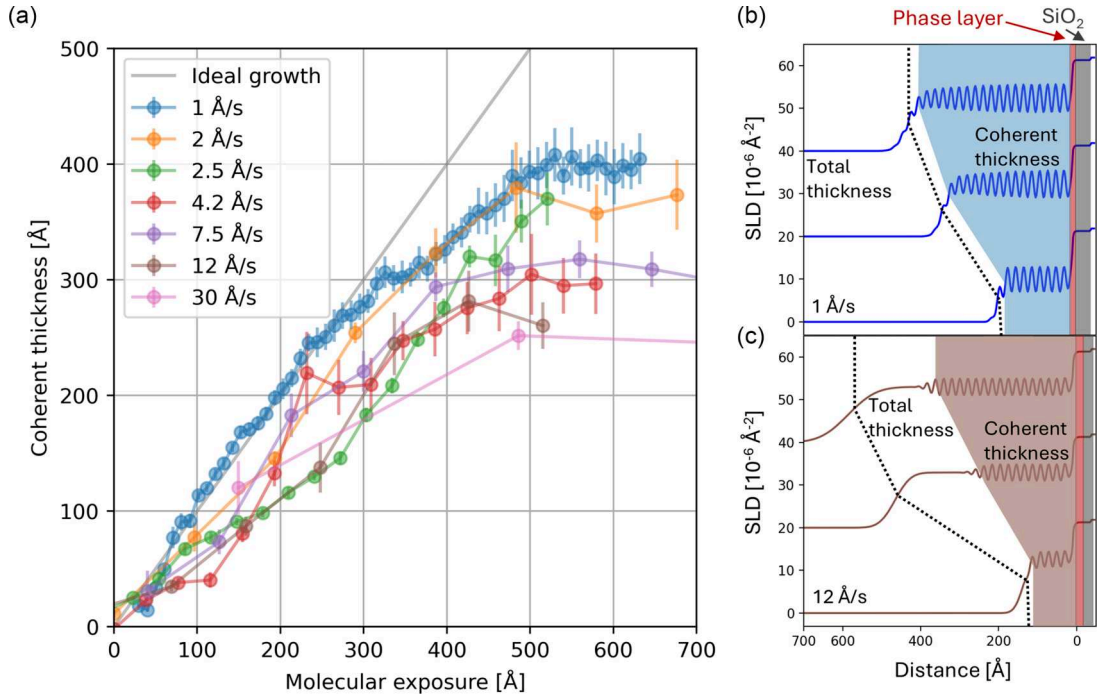

FIG. 4. Thickness of the coherently ordered fraction of the thin film as a function of the molecular exposure for all experiments. (a) Shows that the final coherently ordered film thickness is decreasing with higher growth rates. Moreover, the slope and therefore coherent growth speed is decreasing as well. (b) Three SLD profiles corresponding to slow growth rate of 1 Å/s with coherently ordered layer (colored area) and total thickness of the thin layer (dotted line). (c) SLD profiles for the fast growth rate of 12 Å/s reveal the amorphous layer (250 Å, dotted) on top of the coherently ordered layer (270 Å, colored) at the end of the growth (SLD offset for visualization).

[34,36,40,92], the reason for this rapid roughening may lie in the highly anisotropic shape of molecular PTCDI-C_8 building blocks [see inset of Fig. 1(b)] and in the grain boundaries between grains with different azimuthal orientation. Rod-like molecules with high aspect ratios tend to form rougher films due to their geometry, which affects intermolecular interactions and packing density [36]. Tilt domains which can lead to grain boundaries between grains with different azimuthal orientation reduce the surface mobility of diffusing molecules and significantly influence the structural development of PTCDI-C_8 films. Also, the crossing of step edge barriers from one lattice plane to a lower one is hindered due to the so-called Ehrlich–Schwöbel barrier [40]. Higher barriers than for inorganics have been observed in organic thin films and can influence the roughening of the thin layer [100].

The breakdown of coherent order at higher growth rates can be rationalized by higher deposition rates leading to increased nucleation density, leading to smaller islands and more grain boundaries. These boundaries reduce lateral diffusion, enhancing surface roughening. Molecules growing on grain boundaries often adopt misaligned orientations, disrupting crystallinity. As misaligned crystallites nucleate at these sites, the film becomes increasingly disordered. This defect-rich structure can propagate through subsequent layers, ultimately promoting both roughness and high mosaicity crystalline or amorphous growth.

For films grown at higher deposition rates and thicknesses, we observed deviations in the Bragg peak profile from predictions made by the multilayer model [Figs. S10 and S11(c) [71]]. Specifically, the Bragg peaks appeared less pronounced and broader than expected. Interestingly the coherent thickness estimated from the intensity of the Bragg reflection and the fit through the neural network (NN) agree very well (Fig. S13 [71]). This damping and broadening may be due to the presence of an additional phase or strain within the thin film resulting in Bragg peak splitting. Moreover, the mosaicity and amorphous regions of the thin layer can also contribute to peak broadening, and it is consistent with the measurement indicating smaller coherently ordered fraction of the thin film for higher growth rates. For these reasons of strain or multiple Bragg reflections, the Debye-Scherrer length calculated from broadened peaks does not show a consistent trend with deposition rate. As the XRR measurement is sensitive only to out-of-plane features, any in-plane broadening changes of the Bragg peak are not visible in our fast real-time XRR and rocking scans would be useful for additional information. In conclusion, the coherently ordered layer may not be covered by amorphous material alone, but it can be overlaid also by crystals with varying orientations, varying strain or even another polymorph.

It is important to note that both the high speed x-ray experiments and the machine learning analysis play a crucial role in analyzing noisy and complex datasets to arrive at the above conclusions. Our neural network, trained on a physics-informed model parametrization, accurately predicted the multilayer structures within the films. Thereby it addresses the challenges of overparametrized models and nonunique solutions where traditional fitting methods often falter. The main advantage of the NN is that any correlation between the parameters is obvious during the training of the NN with bad convergence or when the NN is tested on a synthetic test dataset. While differential evolution algorithms

search for a low χ^2 fit to data and often fit smooth lines as a crude and wrong approximation of fast Kiessig oscillations, the NN is looking for Kiessig oscillation shapes within kernel windows. This makes it more sensitive to the oscillations, even when some oscillations are missing due to the absorber edge or the gaps between stitched exposured forming one XRR curve. The NN is also informed though the training data about several q regions of the qXRR curve with the highest noise (absorber edges and beyond Bragg's peak) as the data augmentation was done to mimic real experimental data. Simulating the influence of the absorbers, noise background and gaps between the stripes from multiple detector exposures helps the NN deal with these experimental imperfections.

VII. CONCLUSION

This study demonstrates the effectiveness of employing quick x-ray reflectivity (qXRR) for *in situ* measurements of the fast growth dynamics of PTCDI-C_8 thin films in a high vacuum OMBD environment. We reduce the measurement time for a full high-resolution XRR curve to 12 milliseconds using a typical parallel beam synchrotron beamline setup. With the high time resolution, we overcome the constraints of comparatively slow detector scanning XRR methods that are less suited for studying fast dynamic processes. The innovative qXRR setup allowed us to monitor the evolution of film thickness, density, and interface roughness in real time with fully quantitative fits of the qXRR curves. This study highlights the advantages of using a machine learning approach to handle the vast and noisy datasets typical of qXRR measurements. The neural network's ability to provide near instantaneous, initial parameter guesses greatly improved the efficiency of the fitting process with conventional refnx fits [91,101]. This is particularly valuable in cases where conventional methods struggle, such as with high background noise or sparsely sampled data as well as big data from qXRR.

Through a combination with neural network analysis, we determined the roughening and breakdown of coherent crystalline order of the material as a function of both the film thickness and over more than one order of magnitude variation of the growth from 1 to 30 Å/s. The large range of growth rates enabled us to extend the established scaling relation of roughness with thickness by a phenomenological term describing scaling with growth rate as $\sigma(t, Gr) \sim t^{0.62} \cdot Gr^{0.21}$. The growth exponent β of 0.62 demonstrates a rapid roughening process. Such rapid roughening is indicative of an upward growth phenomenon, aligning with previously observed behaviors in similar organic semiconductor systems like DIP and CuPc [34,38]. Lastly, our investigation into the breakdown of coherent order offers new insights into how the growth rate affects the structural properties of thin films. The reduction in coherent thickness with deposition rate is accompanied by a rise in the amorphous or high mosaicity fraction within the film. The reduction of the coherently ordered layer at faster deposition rates can impact the functional characteristics such as charge carrier or exciton mobilities, and shows that there is a tradeoff between growth speed and film quality in PTCDI-C_8 thin films.

ACKNOWLEDGMENTS

This research was funded in part by the Austrian Science Fund (FWF) Grant No. 10.55776/TAI774. We acknowledge DESY (Hamburg, Germany), a member of the Helmholtz Association HGF, for the provision of experimental facilities at the PETRA III synchrotron light source. We thank Federal Ministry of Education and Research (BMBF) of Germany for funding the employed Eiger2 1M detector via ErUM Pro 05K19FK2 (Murphy, CAU Kiel).

DATA AVAILABILITY

The data that support the findings of this article are openly available [102].

[1] K. Sakurai, M. Mizusawa, and M. Ishii, Recent novel x-ray reflectivity techniques: Moving towards quicker measurement to observe changes at surface and buried interfaces, Trans. Mater. Res. Soc. Jpn. **32**, 181 (2007).

[2] H. Ogawa, H. Masunaga, S. Sasaki, S. Goto, T. Tanaka, T. Seike, S. Takahashi, K. Takeshita, N. Nariyama, K. H. Ohaski *et al.*, Experimental station for multiscale surface structural analyses of soft-material films at SPring-8 via a GISWAX/GIXD/XR-integrated system, Polym. J. **45**, 109 (2013).

[3] H. Joress, J. D. Brock, and A. R. Woll, Quick x-ray reflectivity using monochromatic synchrotron radiation for time-resolved applications, J. Synchrotron Radiat. **25**, 706 (2018).

[4] H. Joress, S. Q. Arlington, T. P. Weihs, J. D. Brock, and A. Woll, X-ray reflectivity with a twist: Quantitative time-resolved x-ray reflectivity using monochromatic synchrotron radiation, Appl. Phys. Lett. **114**, 081904 (2018).

[5] M. Lippmann, A. Buffet, K. Pflaum, A. Ehnes, A. Ciobanu, and O. H. Seeck, A new setup for high resolution fast x-ray reflectivity data acquisition, Rev. Sci. Instrum. **87**, 113904 (2016).

[6] D. Schumi-Mareček, F. Bertram, P. Mikulík, D. Varshney, J. Novák, and S. Kowarik, Millisecond x-ray reflectometry and neural network analysis: Unveiling fast processes in spin coating, J. Appl. Crystallogr. **57**, 314 (2024).

[7] C. Bishop, Neural networks and their applications, Rev. Sci. Instrum. **65**, 1803 (1994).

[8] C. M. Bishop, *Pattern Recognition and Machine Learning* (Springer, New York, 2006).

[9] D. Mareček, J. Oberreiter, A. Nelson, and S. Kowarik, Faster and lower-dose x-ray reflectivity measurements enabled by physics-informed modeling and artificial intelligence co-refinement, J. Appl. Cryst. **55**, 1305 (2022).

[10] L. Pithan, V. Starostin, D. Mareček, L. Petersdorf, C. Volter, V. Munteanu, M. Jankowski, O. Konovalov, A. Gerlach, A. Hinderhofer *et al.*, Closing the loop: Autonomous experiments enabled by machine-learning-based online data analysis in

synchrotron beamline environments, J. Synchrotron Radiat. **30**, 1064 (2023).
[11] V. Munteanu, V. Starostin, A. Greco, L. Pithan, A. Gerlach, A. Hinderhofer, S. Kowarik, and F. Schreiber, Neural network analysis of neutron and x-ray reflectivity data incorporating prior knowledge, J. Appl. Crystallogr. **57**, 456 (2024).
[12] A. R. J. Nelson and S. W. Prescott, refnx: Neutron and x-ray reflectometry analysis in Python, J. Appl. Crystallogr. **52**, 193 (2019).
[13] M. B. Maranville, P. Kienzle, R. Sheridan, M. Doucet, A. J. Caruana, J. Borreguero, A. Nelson, D. P. Hoogerheide, Glass, A. Book, M. Backman, P. P. Balakrishnan, and R. Ghose, reflectometry/refl1d: v1.0.1a1 (Zenodo, 2025), doi:10.5281/zenodo.17651288.
[14] M. Björck and G. Andersson, GenX An extensible x-ray reflectivity refinement program utilizing differential evolution, J. Appl. Cryst. **40**, 1174 (2007).
[15] M. Sawatzki-Park, S.-J. Wang, H. Kleemann, and K. Leo, Highly ordered small molecule organic semiconductor thin-films enabling complex, high-performance multi-junction devices, Chem. Rev. **123**, 8232 (2023).
[16] C. D. Dimitrakopoulos and D. J. Mascaro, Organic thin-film transistors: A review of recent advances, IBM J. Res. Dev. **45**, 11 (2001).
[17] H. Klauk, Organic thin-film transistors, Chem. Soc. Rev. **39**, 2643 (2010).
[18] B. Kumar, B. K. Kaushik, and Y. S. Negi, Perspectives and challenges for organic thin film transistors: Materials, devices, processes and applications, J. Mater. Sci. Mater. Electron. **25**, 1 (2014).
[19] P. Sachan and P. C. Mondal, Coordination-driven opto-electroactive molecular thin films in electronic circuits, J. Mater. Chem. C Mater. **10**, 14532 (2022).
[20] M. Eslamian, Inorganic and organic solution-processed thin film devices, Nano-Micro Lett. **9**, 3 (2017).
[21] C. Li, X. Liu, X. Du, T. Yang, Q. Li, and L. Jin, Preparation and optical properties of nanostructure thin films, Appl. Nanosci. **11**, 1967 (2021).
[22] M. H. Mondal, Study of *in-situ* structural and chemical changes of ultrathin polymer films, Appl. Phys. A **124**, 864 (2018).
[23] M. Lammel, K. Geishendorf, M. A. Choffel, D. M. Hamann, D. C. Johnson, K. Nielsch, and A. Thomas, Fast Fourier transform and multi-Gaussian fitting of XRR data to determine the thickness of ALD grown thin films within the initial growth regime, Appl. Phys. Lett. **117**, 213106 (2020).
[24] J. Xin, P. Sun, F. Zhu, Y. Wang, and D. Yan, Doped crystalline thin-film deep-blue organic light-emitting diodes, J. Mater. Chem. C Mater. **9**, 2236 (2021).
[25] J. P. Spindler, J. W. Hamer, and M. E. Kondakova, OLED manufacturing equipment and methods, in *Handbook of Advanced Lighting Technology* (Springer International Publishing, Cham, 2014), pp. 1–21.
[26] N. N. Dinh, T. S. T. Khanh, L. M. Long, N. D. Cuong, and N. P. H. Nam, Nanomaterials for organic optoelectronic devices: Organic light-emitting diodes, organics solar cells and organic gas sensors, Mater. Trans. **61**, 1422 (2020).
[27] S. R. Forrest, Organic thin film transistors, in *Organic Electronics* (Oxford University Press, Oxford, 2020), pp. 803–917.
[28] X. Guo, F. Yan, P. Cain, T. Nga Ng, W. Tang, R. Sporea, L. Li, J. Carrabina, S. Ogier, A. Perinot *et al.*, Current status and opportunities of organic thin-film transistor technologies, IEEE Trans. Electron Devices **64**, 1906 (2017).
[29] S. Kowarik, A. Gerlach, and F. Schreiber, Organic molecular beam deposition: Fundamentals, growth dynamics, and *in situ* studies, J. Phys. Conden. Mat. **20**, 184005 (2008).
[30] P. Politi, G. Grenet, A. Marty, A. Ponchet, and J. Villain, Instabilities in crystal growth by atomic or molecular beams, Phys. Rep. **324**, 271 (2000).
[31] W. Nunn, T. K. Truttmann, and B. Jalan, A review of molecular-beam epitaxy of wide bandgap complex oxide semiconductors, J. Mater. Res. **36**, 4846 (2021).
[32] S. Das Sarma, C. J. Lanczycki, R. Kotlyar, and S. V. Ghaisas, Scale invariance and dynamical correlations in growth models of molecular beam epitaxy, Phys. Rev. E **53**, 359 (1996).
[33] J. Krug, Four lectures on the physics of crystal growth, Physica A **313**, 47 (2002).
[34] A. C. Dürr, F. Schreiber, K. A. Ritley, V. Kruppa, J. Krug, H. Dosch, and B. Struth, Rapid roughening in thin film growth of an organic semiconductor (Diindenoperylene), Phys. Rev. Lett. **90**, 016104 (2003).
[35] F. Munko, C. C. Luukkonen, I. S. S. Carrasco, F. D. A. A. Reis, and M. Oettel, Island formation in heteroepitaxial growth, Phys. Rev. E **111**, 035501 (2025).
[36] J. T. Dull, X. Chen, H. M. Johnson, M. C. Otani, F. Schreiber, P. Clancy, and B. P. Rand, A comprehensive picture of roughness evolution in organic crystalline growth: The role of molecular aspect ratio, Mater. Horiz. **9**, 2752 (2022).
[37] G. Pradhan, P. P. Dey, and A. K. Sharma, Anomalous kinetic roughening in growth of MoS_2 films under pulsed laser deposition, RSC Adv. **9**, 12895 (2019).
[38] S. Yim and T. S. Jones, Anomalous scaling behavior and surface roughening in molecular thin-film deposition, Phys. Rev. B **73**, 161305 (2006).
[39] N. M. Das, D. Roy, N. Clarke, V. Ganesan, and P. S. Gupta, Dynamics of roughening and growth kinetics of CdS–polyaniline thin films synthesized by the Langmuir–Blodgett technique, RSC Adv. **4**, 32490 (2014).
[40] X. Zhang, E. Barrena, D. Goswami, D. G. de Oteyza, C. Weis, and H. Dosch, Evidence for a layer-dependent Ehrlich-Schwöbel barrier in organic thin film growth, Phys. Rev. Lett. **103**, 136101 (2009).
[41] Y. Zhang, J. Qiao, S. Gao, B. Xu, P. Wang, F. Hu, M. Xiao, Z. Yang, X. Wang, H. Xu *et al.*, Probing carrier transport and structure-property relationship of highly ordered organic semiconductors at the two-dimensional limit, Phys. Rev. Lett. **116**, 016602 (2016).
[42] E. Gann, M. Caironi, Y.-Y. Noh, Y.-H. Kim, and C. R. McNeill, Diffractive x-ray waveguiding reveals orthogonal crystalline stratification in conjugated polymer thin films, Macromolecules **51**, 2979 (2018).
[43] A. Hinderhofer, K. Yonezawa, K. Kato, and F. Schreiber, Structure matters combining x-ray scattering and ultraviolet photoelectron spectroscopy for studying organic thin films, in *Electronic Processes in Organic Electronics*, edited by H. Ishii, K. Kudo, and T. Nakayama (Springer, Tokyo, 2014), pp. 109–129.

[44] Y. Qian, X. Zhang, D. Qi, L. Xie, B. K. Chandran, X. Chen, and W. Huang, Thin-film organic semiconductor devices: From flexibility to ultraflexibility, Sci. China Mater. **59**, 589 (2016).

[45] A. M. Goryaeva, C. Fusco, M. Bugnet, and J. Amodeo, Influence of an amorphous surface layer on the mechanical properties of metallic nanoparticles under compression, Phys. Rev. Mater. **3**, 033606 (2019).

[46] X. Wang, M. Wang, W. Jiang, D. Zhang, H. Wang, and Q. Shan, Mechanical reliability of flexible a-InGaZnO TFTs under dynamic stretch stress, IEEE Trans. Electron Devices **65**, 2863 (2018).

[47] J. Bauri, R. B. Choudhary, and G. Mandal, Recent advances in efficient emissive materials-based OLED applications: A review, J. Mater. Sci. **56**, 18837 (2021).

[48] J. Chen and Q. Zhan, Ellipsometry, in *Handbook of Advanced Nondestructive Evaluation* (Springer International Publishing, Cham, 2019), pp. 513–540.

[49] M. Tolan, *X-Ray Scattering from Soft-Matter Thin Films* (Springer-Verlag, Berlin, Heidelberg, 1999).

[50] P. I. Cohen, P. R. Pukite, J. M. Van Hove, and C. S. Lent, Reflection high energy electron diffraction studies of epitaxial growth on semiconductor surfaces, J. Vac. Sci. Technol. **4**, 1251 (1986).

[51] J. Yu, Y. Xing, Z. Shen, Y. Zhu, D. Neher, N. Koch, and G. Lu, Infrared spectroscopy depth profiling of organic thin films, Mater. Horiz. **8**, 1461 (2021).

[52] S. Festersen, S. B. Hrkac, C. T. Koops, B. Runge, T. Dane, B. M. Murphy, and O. M. Magnussen, X-ray reflectivity from curved liquid interfaces, J. Synchrotron Radiat. **25**, 432 (2018).

[53] U. Pietsch, V. Holý, and T. Baumbach, *High-Resolution X-Ray Scattering* (Springer New York, New York, NY, 2004).

[54] C. Suryanarayana and M. G. Norton, *X-Ray Diffraction* (Springer US, Boston, MA, 1998).

[55] A. Benediktovich, I. Feranchuk, and A. Ulyanenkov, *Theoretical Concepts of X-Ray Nanoscale Analysis* (Springer Berlin Heidelberg, Berlin, Heidelberg, 2014), Vol. 183.

[56] V. Holý, P. Ullrich, and T. Baumbach, *High-Resolution X-Ray Scattering from Thin Films and Multilayers* (Springer Berlin Heidelberg, Berlin, Heidelberg, 1999), Vol. 149.

[57] A. Braslau, P. S. Pershan, G. Swislow, B. M. Ocko, and J. Als-Nielsen, Capillary waves on the surface of simple liquids measured by x-ray reflectivity, Phys. Rev. A (Coll. Park) **38**, 2457 (1988).

[58] M. W. A. Skoda, B. Thomas, M. Hagreen, F. Sebastiani, and C. Pfrang, Simultaneous neutron reflectometry and infrared reflection absorption spectroscopy (IRRAS) study of mixed monolayer reactions at the air-water interface, RSC Adv. **7**, 34208 (2017).

[59] T. P. Russell, X-ray and neutron reflectivity for the investigation of polymers, Materials Science Reports **5**, 171 (1990).

[60] S. Kowarik, A. Gerlach, S. Sellner, F. Schreiber, L. Cavalcanti, and O. Konovalov, Real-time observation of structural and orientational transitions during growth of organic thin films, Phys. Rev. Lett. **96**, 125504 (2006).

[61] J. Daillant and A. Gibaud, *X-Ray and Neuron Reflectivity: Principles and Applications* (Springer Berlin Heidelberg, Berlin, Heidelberg, 1999), Vol. 58.

[62] K. Lament, M. Grodzicki, R. Wasielewski, P. Mazur, and A. Ciszewski, Growth and properties of ultra-thin PTCDI-C_8 films on GaN(0001), Crystals (Basel) **14**, 201 (2024).

[63] A. Zykov, S. Bommel, C. Wolf, L. Pithan, C. Weber, P. Beyer, G. Santoro, J. P. Rabe, and S. Kowarik, Diffusion and nucleation in multilayer growth of PTCDI-C_8 studied with *in situ* x-ray growth oscillations and real-time small angle x-ray scattering, J. Chem. Phys. **146**, 052803 (2017).

[64] T. N. Krauss, E. Barrena, X. N. Zhang, D. G. de Oteyza, J. Major, V. Dehm, F. Würthner, L. P. Cavalcanti, and H. Dosch, Three-dimensional molecular packing of thin organic films of PTCDI-C_8 determined by surface x-ray diffraction, Langmuir **24**, 12742 (2008).

[65] G. Witte and C. Wöll, Growth of aromatic molecules on solid substrates for applications in organic electronics, J. Mater. Res. **19**, 1889 (2004).

[66] R. J. Chesterfield, J. C. McKeen, C. R. Newman, P. C. Ewbank, D. A. da Silva Filho, J.-L. Brédas, L. L. Miller, K. R. Mann, and C. D. Frisbie, Organic thin film transistors based on N -Alkyl perylene diimides: Charge transport kinetics as a function of gate voltage and temperature, J. Phys. Chem. B **108**, 19281 (2004).

[67] D. J. Gundlach, K. P. Pernstich, G. Wilckens, M. Grüter, S. Haas, and B. Batlogg, High mobility *n*-channel organic thin-film transistors and complementary inverters, J. Appl. Phys. **98**, 064502 (2005).

[68] S. Tatemichi, M. Ichikawa, T. Koyama, and Y. Taniguchi, High mobility *n*-type thin-film transistors based on *N,N′*-ditridecyl perylene diimide with thermal treatments, Appl. Phys. Lett. **89**, 112108 (2006).

[69] C. Rolin, K. Vasseur, S. Schols, M. Jouk, G. Duhoux, R. Müller, J. Genoe, and P. Heremans, High mobility electron-conducting thin-film transistors by organic vapor phase deposition, Appl. Phys. Lett. **93**, 033305 (2008).

[70] O. H. Seeck, H. Franz, F. Bertam, M. Greve, A. Beerlink, K. Pflaum, B. M. Murphy, H. Schulte-Schrepping, O. Magnussen, C. Deiter *et al.*, The high-resolution diffraction beamline P08 at PETRA III, J. Synchrotron Radiat. **19**, 30 (2012).

[71] See Supplemental Material at http://link.aps.org/supplemental/10.1103/xxx9-8tk2 for details.

[72] K. A. Ritley, B. Krause, F. Schreiber, and H. Dosch, A portable ultrahigh vacuum organic molecular beam deposition system for *in situ* x-ray diffraction measurements, Rev. Sci. Instrum. **72**, 1453 (2001).

[73] S. R. Forrest, Ultrathin organic films grown by organic molecular beam deposition and related techniques, Chem. Rev. **97**, 1793 (1997).

[74] O. Filies, O. Böling, K. Grewer, J. Lekki, M. Lekka, Z. Stachura, and B. Cleff, Surface roughness of thin layers—a comparison of XRR and SFM measurements, Appl. Surf. Sci. **141**, 357 (1999).

[75] P. R. Nayak, Random process model of rough surfaces, J. Lubr. Technol. **93**, 398 (1971).

[76] T. Velinov, L. Ahtapodov, A. Nelson, M. Gateshki, and M. Bivolarska, Influence of the surface roughness on the properties of Au films measured by surface plasmon resonance and x-ray reflectometry, Thin. Solid. Films **519**, 2093 (2011).

[77] Y. LeCun, Y. Bengio, and G. Hinton, Deep learning, Nature (London) **521**, 436 (2015).

[78] K. He, X. Zhang, S. Ren, and J. Sun, Deep residual learning for image recognition, in *2016 IEEE Conference on Computer Vision and Pattern Recognition (CVPR)* (IEEE, Piscataway, NJ, 2016), pp. 770–778.

[79] G. Huang, Z. Liu, L. van der Maaten, and K. Q. Weinberger, Densely connected convolutional networks, in *2017 IEEE Conference on Computer Vision and Pattern Recognition (CVPR)* (IEEE, Piscataway, NJ, 2017), pp. 2261–2269.

[80] M. Tan and Q. Le, EfficientNet: Rethinking model scaling for convolutional neural networks, in *Proceedings of the 36th International Conference on Machine Learning*, edited by K. Chaudhuri, and R. Salakhutdinov, Vol. 97 (PMLR, 2019), pp. 6105–6114.

[81] F. Murtagh, Multilayer perceptrons for classification and regression, Neurocomputing **2**, 183 (1991).

[82] D. Hendrycks and K. Gimpel, Gaussian error linear units (GELUs), arXiv:1606.08415.

[83] D. P. Kingma and J. Ba, Adam: A method for stochastic optimization, *3rd International Conference on Learning Representations, ICLR 2015 - Conference Track Proceedings 1* (ICLR, 2014).

[84] M. Abadi, P. Barham, J. Chen, Z. Chen, A. Davis, J. Dean, M. Devin, S. Ghemawat, G. Irving, M. Isard *et al.*, TensorFlow: A System for Large-Scale Machine Learning, in *OSDI'16: Proceedings of the 12th USENIX conference on Operating Systems Design and Implementation* (ACM, 2016), pp. 265–283.

[85] A. Greco, V. Starostin, C. Karapanagiotis, A. Hinderhofer, A. Gerlach, L. Pithan, S. Liehr, F. Schreiber, and S. Kowarik, Fast fitting of reflectivity data of growing thin films using neural networks, J. Appl. Crystallogr. **52**, 1342 (2019).

[86] A. Greco, V. Starostin, A. Hinderhofer, A. Gerlach, M. W. A. Skoda, S. Kowarik, and F. Schreiber, Neural network analysis of neutron and x-ray reflectivity data: Pathological cases, performance and perspectives, Mach. Learn Sci. Technol. **2**, 1 (2021).

[87] D. Mironov, J. H. Durant, R. Mackenzie, and J. F. K. Cooper, Towards automated analysis for neutron reflectivity, Mach. Learn Sci. Technol. **2**, 035006 (2021).

[88] M. Doucet, R. K. Archibald, and W. T. Heller, Machine learning for neutron reflectometry data analysis of two-layer thin films, Mach. Learn Sci. Technol. **2**, 035001 (2021).

[89] J. M. C. Loaiza and Z. Raza, Towards reflectivity profile inversion through artificial neural networks, Mach. Learn Sci. Technol. **2**, 025034 (2021).

[90] Z. Chen, N. Andrejevic, N. C. Drucker, T. Nguyen, R. P. Xian, T. Smidt, Y. Wang, R. Ernstorfer, D. A. Tennant, M. Chan *et al.*, Machine learning on neutron and x-ray scattering and spectroscopies, Chem. Phys. Rev. **2**, 031301 (2021).

[91] V. Starostin, M. Dax, A. Gerlach, A. Hinderhofer, Á. Tejero-Cantero, and F. Schreiber, Fast and reliable probabilistic reflectometry inversion with prior-amortized neural posterior estimation, Sci. Adv. **11**, eadr9668 (2024).

[92] J. Yang, S. Yim, and T. S. Jones, Molecular-orientation-induced rapid roughening and morphology transition in organic semiconductor thin-film growth, Sci. Rep. **5**, 9441 (2015).

[93] A.-L. Barabási and H. E. Stanley, *Fractal Concepts in Surface Growth* (Cambridge University Press, Cambridge, 1995).

[94] F. Family and T. Vicsek, Scaling of the active zone in the Eden process on percolation networks and the ballistic deposition model, J. Phys. A Math Gen. **18**, L75 (1985).

[95] T. Vicsek and F. Family, Dynamic scaling for aggregation of clusters, Phys. Rev. Lett. **52**, 1669 (1984).

[96] F. L. Forgerini and R. Marchiori, A brief review of mathematical models of thin film growth and surfaces, Biomatter **4**, e28871 (2014).

[97] K. Bordo and H.-G. Rubahn, Effect of deposition rate on structure and surface morphology of thin evaporated al films on dielectrics and semiconductors, Mater. Sci. **18**, 392 (2012).

[98] D. G. Foster, Y. Shapir, and J. Jorne, The effect of rate of surface growth on roughness scaling, J. Electrochem. Soc. **152**, C462 (2005).

[99] J. Krug, Origins of scale invariance in growth processes, Adv. Phys. **46**, 139 (1997).

[100] G. Hlawacek, P. Puschnig, P. Frank, A. Winkler, C. Ambrosch-Draxl, and C. Teichert, Characterization of step-edge barriers in organic thin-film growth, Science **321**, 108 (2008).

[101] A. Greco, N. Rußegger, A. Hinderhofer, E. Edel, F. Schreiber, V. Starostin, V. Munteanu, A. Gerlach, I. Dax, C. Shen *et al.*, Neural network analysis of neutron and x-ray reflectivity data: Automated analysis using mlreflect, experimental errors and feature engineering, J. Appl. Crystallogr. **55**, 362 (2022).

[102] D. Schumi-Mareček, M. Haberl, A. Nelson, E. Pfeiler, M. Eder, F. Bertram, and S. Kowarik, "High-speed x-ray reflectometry dataset for PTCDI-C_8 molecules" [Data set], Zenodo (2025), https://doi.org/10.5281/zenodo.17340970.